On the threedimensional instability of a swirling, annular, inviscid liquid sheet subject to unequal gas velocities

Mahesh V. Panchagnula, Paul E. Sojka, and Philip J. Santangelo

Citation: Physics of Fluids (1994-present) **8**, 3300 (1996); doi: 10.1063/1.869119
View online: http://dx.doi.org/10.1063/1.869119
View Table of Contents: http://scitation.aip.org/content/aip/journal/pof2/8/12?ver=pdfcov
Published by the AIP Publishing

On the three-dimensional instability of a swirling, annular, inviscid liquid sheet subject to unequal gas velocities

Mahesh V. Panchagnula, Paul E. Sojka,[a] and Philip J. Santangelo
Thermal Sciences and Propulsion Center, School of Mechanical Engineering, Purdue University, West Lafayette, Indiana 47907-1003

(Received 13 May 1996; accepted 19 August 1996)

A linear model describing the instability behavior of annular, swirling, inviscid sheets subject to inner and outer gas flows of differing velocities is presented. The model considers three-dimensional disturbances and contains previous flat sheet, cylindrical jet, and annular jet analyses as limiting cases. Model predictions show that, in the absence of swirl, (i) an increase in axial Weber number causes the range of unstable axial disturbance modes to increase, (ii) when the axial Weber numbers are small (<8), inner gas flows lead to slightly faster growing axial instability modes than outer gas flows at equivalent inner and outer Weber numbers, but inner and outer gas flows have the same effect when Weber numbers are high (>10), (iii) the wavenumber for the axial mode having the highest growth rate decreases with a decrease in axial Weber number, (iv) an increase in the density of the atomizing gas results in a slight increase in the wavenumber of the axial disturbance mode having the highest growth rate. When swirl is present, model predictions demonstrate that (v) swirl reduces the wavenumber for the axial disturbance mode having the highest growth rate and reduces growth rates as well, (vi) an increase in the swirl Weber number beyond the stabilizing region increases the range of unstable axial and circumferential modes and increases growth rates as well for nonzero axial Weber numbers, (vii) increasing the swirl Weber number increases the axial wavenumber for the disturbance mode having the highest growth rate, but a circumferential mode number of zero is retained until the swirl Weber number exceeds about 8, at which point the axial wavenumber for the disturbance having the highest growth rate falls to zero and the circumferential wavenumber jumps to a finite value of n at which time further increases in swirl Weber number serve to increase n, (viii) up to two local nondimensional growth rate maxima can exist, and the instability domain can be simply connected or can consist of two separate regions separated by an area where disturbances are stable. The topology of the growth rate surface depends on the ratio of the annulus inner to outer radii. These findings are used to explain some observations of practical atomizer performance. © *1996 American Institute of Physics.* [S1070-6631(96)01012-4]

I. INTRODUCTION

Annular liquid sheet stability has been the subject of research since Ponstein's[1] study over 30 years ago. Annular liquid sheet stability is of importance both from a practical and a theoretical point of view.

From a practical view point, annular liquid sheets are known to be formed in various liquid spray applications.[2] Spray formation through the breakup of an annular liquid sheet has been found to be an efficient process[2] because of the increased surface area for interaction between the gas and the liquid. Many practical atomizers, including pressure swirl, airblast, air assist, pre-filming airblast and effervescent, utilize this fact. Therefore, it is important to understand the stability of annular liquid sheets.

Annular liquid sheet stability is also of interest from a theoretical view point. A swirling annular sheet is the most general two-dimensional geometry and other common geometries, such as the cylindrical jet, the plane sheet, the hollow jet, and the nonswirling annular sheet, can be treated as special cases.[1] As a result, the information obtained from this analysis will be useful in a variety of applications.

Annular liquid sheets have been studied experimentally by a number of researchers. Recently, Santangelo and Sojka[3] used focused image holography (FIH) to investigate the Weber number-dependent breakup of an annular sheet formed in the near nozzle region of an effervescent atomizer produced spray. Figure 1 is an artist's rendition reflecting a typical holographic image. As can be seen, the liquid exits the nozzle in the form of an annular sheet with a coflowing gas core. The sheet undergoes circumferential breakup and evolves into a finite number of ligaments close to the nozzle. The ligaments are themselves unstable and undergo axial breakup into drops. This breakup process is clearly multidimensional.

This multidimensional process is fundamentally different from what previous experimental researchers of annular liquid sheets[4,5] have found. Kendall[4] and Lee[5] studied low mass flow rate, low Weber number annular jets and found that the jets developed axisymmetric disturbances and that the liquid broke up into spherical shells with gas trapped inside them. The process of shell formation observed by Kendall[4] and Lee[5] at low Weber numbers and the process of effervescent spray formation observed by Santangelo and Sojka[3] at high Weber numbers are based on the same phenomenon, viz., annular sheet instability, but are qualitatively distinct. Any model that successfully describes the annular

[a]Telephone: (317) 494-1536; Fax: (317)494-0530; Electronic mail: sojka@ecn.purdue.edu

 1070-6631/96/8(12)/3300/13/$10.00

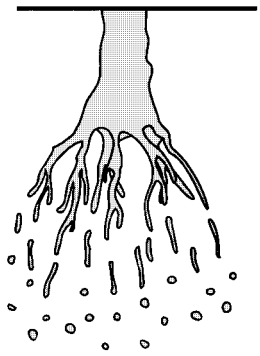

FIG. 1. Artist's rendition of a near-nozzle structure hologram [Santangelo and Sojka (1993)].

sheet instability process must be able to explain this difference.

As is obvious from Fig. 1, effervescent spray near nozzle structure is three dimensional, i.e., it has a distinct circumferential breakup pattern along with a longitudinal structure. This circumferential behavior cannot be predicted by an axisymmetric instability analysis. A model accounting for the growth of circumferential disturbances must be formulated to predict this structure, since no such models exist. The goal of the present work is to study the stability of an annular, swirling, inviscid liquid sheet subject to unequal gas velocities inside and outside and to develop a model to predict the qualitatively different breakup structures observed by Kendall[4] and Santangelo and Sojka.[3]

The model described here is restricted to inviscid applications. Practical examples include sprays formed from low-viscosity liquids such as commercial diesel fuel, aviation fuels, automobile fuels, plus glass cleaners, and water in fire suppression/explosion control systems. Liquid viscosity can be important in some cases. Previous studies of instability for other geometries have shown that viscosity can be important when the disturbance wavelength is small compared to the sheet thickness. Such behavior might be expected to occur at high Weber numbers.

A number of previous studies are pertinent to this investigation. Table I provides a summary of this body of research. The first study of annular sheet stability was reported by Ponstein.[1] He derived the general dispersion relation for the growth of disturbances under the influence of a potential swirl flow and a uniform axial mean velocity, while neglecting the effects of viscosity and the presence of the two gas phases. Ponstein[1] showed that the annular sheet is stable to nonaxisymmetric disturbances in the absence of swirl. He also showed that swirl can cause circumferential modes of wavenumber greater than zero to be more unstable than the axisymmetric mode.

Subsequent researchers[6–11] studied the stability of annular liquid sheets and found that the curvature of the sheet has a significant impact on its stability. As a consequence, existing relations from flat sheet stability analyses[12] cannot be used to predict the breakup of an annular sheet. In addition, the annular sheet analyses[6–11] were two dimensional and neglected one or more effects (liquid viscosity, or the gas phase inside, or the gas phase outside, or swirl, or circumferential disturbances). These models are therefore incapable of predicting the three-dimensional near-nozzle flow structure observed by Santangelo and Sojka.[3]

Panchagnula *et al.*[13] developed a linear instability model of an annular liquid sheet including the effects of liquid surface tension and gas phase inertia inside and outside the sheet, and accounted for nonaxisymmetric instability modes. They found that the range of unstable modes in both the axial and circumferential directions, increases as the Weber num-

TABLE I. Annular sheet stability literature summary.

Researcher(s)	Viscous/Inviscid	Disturbance mode	Swirl/no swirl	Gas phases
Ponstein[1]	Inviscid liquid	Nonaxisymmetric and axial disturbances	Swirling liquid	Gas presence neglected
Dumbleton and Hermans[6]	Inviscid liquid	Axisymmetric and axial disturbances	No swirl	Gas presence neglected
Crapper *et al.*[7]	Inviscid liquid	Axisymmetric and axial disturbances	No swirl	Gas phases at rest
Esser *et al.*[8]	Inviscid liquid	Nonaxisymmetric and axial disturbances	No swirl	Gas phases at rest
Meyer and Weihs[9]	Viscous liquid	Axisymmetric and axial disturbances	No swirl	Gas phases at rest
Harvanek and Chow[10]	Viscous liquid	Axisymmetric and axial disturbances	No swirl	Ambient gas at rest
Radwan[21]	Inviscid liquid	Axisymmetric disturbances	No swirl	Ambient gas at rest
Radwan[22]	Inviscid liquid	Axisymmetric disturbances	No swirl	Both gas phases at same velocity
Shen and Li[16]	Viscous liquid	Axisymmetric and axial disturbances	No swirl	Gas phases at different velocities
Present work	Inviscid liquid	Nonaxisymmetric and axial disturbances	Swirl	Gas phases at different velocities

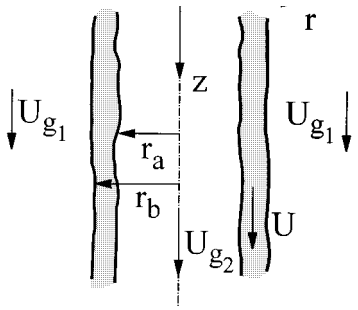

FIG. 2. Geometry and nomenclature of annular liquid flow.

ber increases and, therefore, any assumptions of axial symmetry could lead to incorrect conclusions.

In summary, previous studies do not address the general case of three-dimensional annular sheet instability for a swirling liquid in the presence of inner and outer gas phases of differing velocities. As such, they cannot hope to predict the experimentally observed multidimensional instabilities. We address that lack in the present work.

II. MODEL AND GOVERNING EQUATIONS

Figure 2 illustrates the geometry and the flow parameters being considered in this analysis. The temporal instability of an infinitely long annular liquid sheet in the presence of gas flows inside and outside the sheet is investigated. The gas and the liquid flows are assumed to be incompressible and the mean velocity distributions uniform and steady. The coordinate system is held stationary with respect to the nozzle.

The equations governing the flow are the momentum equations in the r, θ, and z directions, along with continuity,

$$\frac{\partial \mathbf{V}_j}{\partial t}+(\mathbf{V}_j\cdot\boldsymbol{\nabla})\mathbf{V}_j=-\frac{1}{\rho_j}\boldsymbol{\nabla}p_j, \tag{1}$$

$$\boldsymbol{\nabla}\cdot\mathbf{V}_j=0. \tag{2}$$

Here, $j=i$, l, and o correspond to the gas phase inside the annulus, the liquid phase, and the gas phase outside the annulus, respectively.

One set of boundary conditions, termed the dynamic boundary conditions, is given by the stress tensor continuity requirement across the gas–liquid interfaces,

$$\sum \sigma_{rr}=0. \tag{3}$$

The other set of boundary conditions, known as the kinematic boundary condition, arises from the fact that any particle on a fluid surface remains on that surface at all times

$$\frac{D(r-\eta)}{Dt}=0, \tag{4}$$

evaluated on the two free surfaces. Here η is the disturbance imposed on the free surface.

The steady flow is perturbed and the governing equations and boundary conditions are linearized with respect to the perturbation. A normal mode form is assumed for the perturbation since the sheet is infinite in the z direction and periodic in the θ direction. For example the perturbation velocity in the gas phase inside the annulus can be written as

$$u_j=\hat{u}_j\cdot\exp(\omega t+ikz+in\theta), \tag{5}$$

where k and n are the wave numbers of the perturbation in the z and θ directions, respectively, ω is the temporal growth rate, and t is the time. The governing equations and boundary conditions are solved to yield the eigenvalue ω as a function of k and n and the other fluid flow parameters (the nondimensional densities, the Weber numbers, the ratio of the radii of the annular sheet, plus the nondimensional velocities of all three streams).

A. Linear stability analysis of an inviscid, swirling, annular sheet

Consider an inviscid annular sheet moving with a uniform axial velocity and a mean swirl velocity described by A/r, where A is the strength of the swirl vortex. The mean flows in the three phases, gas phase inside, the liquid phase, and the gas phase outside, are therefore given by $[0,0,W_i]$, $[0, A/r, W_l]$, and $[0,0,W_o]$. This form of flow is known to occur in swirl atomizer applications.[14]

Applying a force balance to this configuration, we obtain the necessary condition for the existence of this flow,

$$P_i-P_o=\sigma\left(\frac{1}{r_a}+\frac{1}{r_b}\right)-\frac{1}{2}\rho_l A^2\left(\frac{1}{r_a^2}-\frac{1}{r_b^2}\right), \tag{6}$$

with r_a and r_b as given in Fig. 2. Equation (6) is the mean pressure matched condition for inviscid swirling flow and requires that the forces due to surface tension, gas phase, and liquid pressures, and the centrifugal force due to the swirling motion balance each other.

This flow is now perturbed and the growth or decay of the disturbance is examined as a function of the wave number of the perturbation. For example, the total axial velocity in the liquid phase is given by $W=W_l+w_l$, where w_l is the perturbation velocity. This form is substituted into the governing equations (1) and (2) for all velocities. Equation (1) is then linearized to yield the system of equations describing the perturbation growth,

$$\left(\frac{\partial}{\partial t}+W_i\frac{\partial}{\partial z}\right)\mathbf{u}_i=-\frac{1}{\rho_i}\boldsymbol{\nabla}p_i, \tag{7a}$$

$$\left(\frac{\partial}{\partial t}+\frac{A}{r^2}\frac{\partial}{\partial\theta}+W_l\frac{\partial}{\partial z}\right)\mathbf{u}_l=-\frac{1}{\rho_l}\boldsymbol{\nabla}p_l, \tag{7b}$$

$$\left(\frac{\partial}{\partial t}+W_o\frac{\partial}{\partial z}\right)\mathbf{u}_o=-\frac{1}{\rho_0}\boldsymbol{\nabla}p_o, \tag{7c}$$

$$\boldsymbol{\nabla}\cdot\mathbf{u}_i=0, \tag{8a}$$

$$\boldsymbol{\nabla}\cdot\mathbf{u}_l=0, \tag{8b}$$

$$\boldsymbol{\nabla}\cdot\mathbf{u}_o=0, \tag{8c}$$

where $\mathbf{u}$ is the perturbation velocity vector and p the perturbation pressure. The kinematic boundary conditions for the gas and liquid are given by

$$u_i=\frac{\partial\eta_i}{\partial t}+W_i\frac{\partial\eta_i}{\partial z},\quad \text{at } r=r_a, \tag{9a}$$

$$u_o=\frac{\partial \eta_o}{\partial t}+W_0\,\frac{\partial \eta_o}{\partial z},\quad \text{at } r=r_b, \tag{9b}$$

$$u_l=\left(\frac{\partial}{\partial t}+\frac{A}{r^2}\,\frac{\partial}{\partial \theta}+W_l\,\frac{\partial}{\partial z}\right)\eta_i,\quad \text{at } r=r_a, \tag{10a}$$

$$u_l=\left(\frac{\partial}{\partial t}+\frac{A}{r^2}\,\frac{\partial}{\partial \theta}+W_l\,\frac{\partial}{\partial z}\right)\eta_o,\quad \text{at } r=r_b. \tag{10b}$$

The dynamic boundary conditions are given by

$$-p_l-\rho_l\,\frac{A^2}{r_a^3}\,\eta_i=-\sigma\left(\frac{\eta_i}{r_a^2}+\frac{1}{r_a^2}\,\frac{\partial^2\eta_i}{\partial\theta^2}+\frac{\partial^2\eta_i}{\partial z^2}\right)-p_i,$$

$$\text{at } r=r_a, \tag{11a}$$

$$-p_l-\rho_l\,\frac{A^2}{r_b^3}\,\eta_o=\sigma\left(\frac{\eta_o}{r_b^2}+\frac{1}{r_b^2}\,\frac{\partial^2\eta_o}{\partial\theta^2}+\frac{\partial^2\eta_o}{\partial z^2}\right)-p_0,$$

$$\text{at } r=r_b. \tag{11b}$$

The resulting governing equations and boundary conditions are nondimensionalized using a characteristic time, length, and mass of the system,

$$[T]:=\sqrt{\frac{\rho_l r_b^3}{\sigma}}, \tag{12a}$$

$$[L]:=r_b, \tag{12b}$$

$$[M]:=\rho_l r_b^3. \tag{12c}$$

This results in a set of dimensionless parameters,

$$\mathrm{We}_i=\frac{\rho_i U_i^2 r_a}{\sigma}, \tag{13a}$$

$$\mathrm{We}_o=\frac{\rho_o U_o^2 r_b}{\sigma}, \tag{13b}$$

$$\mathrm{We}_s=\frac{\rho_l A^2}{\sigma r_b}, \tag{13c}$$

$$g_i=\frac{\rho_i}{\rho_l}, \tag{14a}$$

$$g_o=\frac{\rho_o}{\rho_l}, \tag{14b}$$

$$\gamma=\frac{r_a}{r_b}. \tag{15}$$

Here We_i is the Weber number inside, We_o is the Weber number outside, and We_s is the swirl Weber number. Here g_i is the gas-to-liquid phase density ratio for the gas inside the sheet, g_o is the gas-to-liquid phase density ratio for the gas outside the sheet, and γ is the ratio of the annular sheet inner and outer radii.

Two modes of instability are known to exist—the symmetric and the antisymmetric. Recent work by Shen and Li[15] has shown that the growth rates for the antisymmetric, or parasinuous, mode are an order of magnitude greater than those for the symmetric, or paravaricose, mode when the density ratio is of the order of 0.01 or less. The dominance of the parasinuous mode has also been observed experimentally by Kendall[4] and by Santangelo and Sojka.[3] We have therefore chosen to consider only the antisymmetric mode.

The solution to this problem is sought under the normal mode assumption for the perturbation velocities, pressures and surface disturbances. This results in a characteristic equation for the eigenvalue, ω, as a function of the fluid properties, ρ and σ, mean velocities, W_i, W_o, and W_l, the geometry of the flow, γ, and the axial and circumferential wavenumbers, k and n. The characteristic equation, also known as the dispersion relation, is a polynomial of fourth order,

$$a_4(k,n)\omega^4+a_3(k,n)\omega^3+a_2(k,n)\omega^2+a_1(k,n)\omega+a_0(k,n)=0. \tag{16}$$

The coefficients $\{a_i\}$ are presented explicitly in Appendix A. This equation was solved for any assumed pair of wavenumbers (k,n) using MATLAB™. The root with the largest real part was assumed to be the growth rate of the disturbance corresponding to the favored axial and circumferential mode because the disturbances are assumed to grow exponentially. The variation in favored growth rate was then plotted as a function of k and n. The mode corresponding to the maximum value of ω is referred to as the optimal disturbance mode. This peak value, which occurs at a certain value of k and n, is assumed to dominate the breakup process assuming that no disturbance mode is favored heavily in the initial perturbation and that the waves grow exponentially.

Finally, the variation in peak growth rate and optimal disturbance mode with the parameters We_i, We_o, We_s, g_i, g_o, and γ was studied over a range of engineering interest.

B. Verification of the dispersion relation

The dispersion equation presented in the previous section has been verified against relations derived during previous linear analyses[5,9,15,16] by letting the pertinent parameters tend to their asymptotic limits and analytically verifying the resulting expressions. For example, Eq. (16) reduces to the plane sheet expressions of Rangel and Sirignano[16] and Shen and Li[15] in the limiting case where the inner and outer annulus radii tend to infinity while the sheet thickness remains finite. In addition, Eq. (16) reduces to the *inviscid* limit of the Meyer and Weihs[9] expression (originally derived for a nonswirling, viscous, annular sheet) when the circumferential mode number, n, and the viscosity are identically set to zero. This occurs because the Bessel functions $K_{n-1}(lr)$ and $K_{n+1}(lr)$ are both equal to $K_1(lr)$ when $n=0$. Meyer and Weihs[9] have verified that their dispersion equation reduces to the expression of Sterling and Sleicher[17] for a cylindrical jet when $r_a\to 0$. They were also able to reduce their equation to the hollow jet growth rate equation given by Chandrasekhar[18] when $r_b\to\infty$. When the ratio of the radii r_a/r_b approaches unity and when the viscosity tends to zero, Meyer and Weihs[9] were able to recover the expression for a thin inviscid sheet derived by Squire.[19] Consequently, our analysis will also reduce to the cylindrical jet, hollow jet and plane sheet cases in the appropriate limits. Finally, Eq. (16)

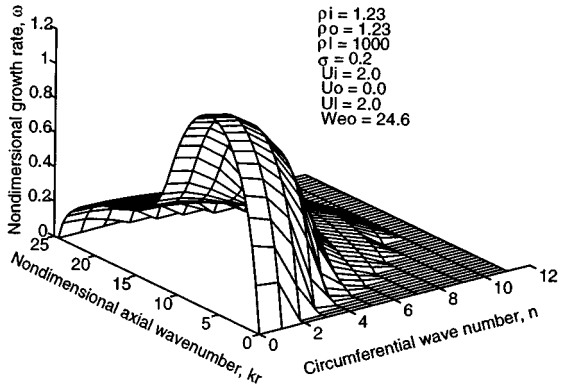

FIG. 3. Growth rate versus nondimensional axial and circumferential wavenumbers at $We_o=24.6$.

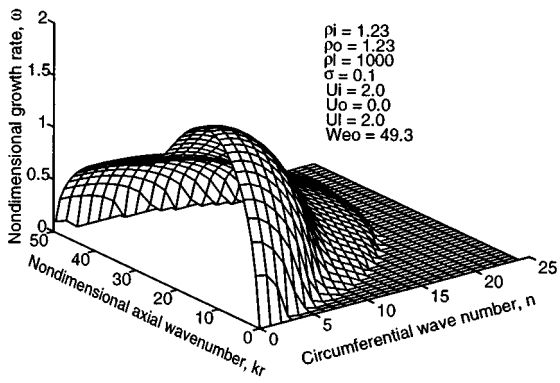

FIG. 4. Growth rate versus nondimensional axial and circumferential wavenumbers at $We_o=49.3$.

is observed to reduce to the dispersion equation of Ponstein[1] when the densities of the gas medium inside and outside the annular sheet are set equal to zero.

In summary, our dispersion equation has been checked against existing relations to ensure that it can be reduced to all of the correct asymptotic limits, viz., a cylindrical jet, a plane sheet, a hollow jet, a nonswirling annular sheet, and a swirling sheet in the absence of a gas phase. Results obtained by analyzing the general form of the dispersion relation are presented in the next section.

III. RESULTS AND DISCUSSION

The dispersion relation derived for inviscid swirling annular sheets was analyzed for unstable disturbance modes. Effects of inside and outside Weber number, swirl Weber number, and gas-phase-to-liquid-phase density ratios were considered. In each case the dispersion equation was solved for the growth rate by calculating all its roots. The root with the maximum real part was assumed to dominate since the waves were assumed to grow exponentially. All results are presented in terms of the dimensionless growth rate, ω, the dimensionless axial wavenumber, kr_b, the dimensionless circumferential wavenumber, n, the annular sheet radii ratio, γ, the Weber numbers for the gas flow inside, gas flow outside, and swirling liquid flow (We_i, We_o, and We_s, respectively), plus the inner gas and outer gas density ratios, g_i and g_o.

A. Effect of We_i and We_o when $We_s=0$

The effect of variations in both inside and outside axial Weber numbers, We_i and We_o, was studied with the swirl Weber number, We_s, set equal to zero. As will be shown, the effects of We_i and We_o are qualitatively similar for high Weber numbers. Therefore, the inside Weber number was set to zero in Figs. 3 and 4 to illustrate qualitative details in the dispersion diagram.

Figure 3 is a plot of the nondimensional growth rate versus the nondimensional axial and circumferential wavenumbers, kr_b and n, at an outside Weber number, We_o, of 24.6, with $g_i=g_o=0.001\,23$ and $\gamma=0.99$. This flow condition is representative of typical atomizer flow conditions, where the annular sheet is thin and the Weber numbers are moderate. As can be seen, there is a range of axial and circumferential wavenumbers that are unstable. However, the optimal disturbance mode corresponds to $n=0$ and a positive value for the nondimensional axial wavenumber. In addition, it was found that there exists a critical Weber number, We*, for each nonaxisymmetric mode to become unstable. For example, $We_o=24.6$ corresponds to the critical Weber number for the $n=10$ mode in Fig. 3.

Figure 4 is a plot similar to Fig. 3, except that We_o is doubled. As can be seen, the range of unstable axial and circumferential wavenumbers is approximately doubled and the growth rates of the various disturbance modes are noticeably higher than those of Fig. 3. This is because the destabilizing aerodynamic forces dominate the stability behavior as We_o goes up. More importantly, the optimal wavenumber is higher in Fig. 4 than in Fig. 3 ($kr_b\sim7$ in Fig. 3, as opposed to ~15 in Fig. 4). This means that the wavelength at breakup decreases with an increase in surface tension. The practical implication of this conclusion is that drops produced by ligaments breaking up under this mechanism will have smaller diameters as the Weber number increases. This agrees qualitatively with the near nozzle structure of effervescent atomizer produced sprays, as observed by Santangelo and Sojka,[3] and with the experimental results of Lee.[5]

In conclusion, we see that as the Weber number increases, the range of instability in the axial and circumferential directions and the optimal wavenumber in the axial direction all increase, while retaining the $n=0$ mode as the fastest growing disturbance. This result is consistent with the experimental findings of Kendall[5] and Lee.[4] Finally, the influence of surface tension on breakup follows that of the one-dimensional disturbance case—an increase in σ leads to an increase in optimal wavelength.

Figures 5(a) and 5(b) are plots of the nondimensional axial wavenumber and the corresponding growth rate versus We_i/γ. The quotient We_i/γ was chosen for one of the axes to isolate the aerodynamic effect of the gas phases. This arises from the definition of We_i and We_o [see Eq. (13)].

Three distinct regions can be observed in Fig. 5(a). Regions at low and high We_i/γ quotients can be identified where the curves for each of the four radii ratio fall on top of

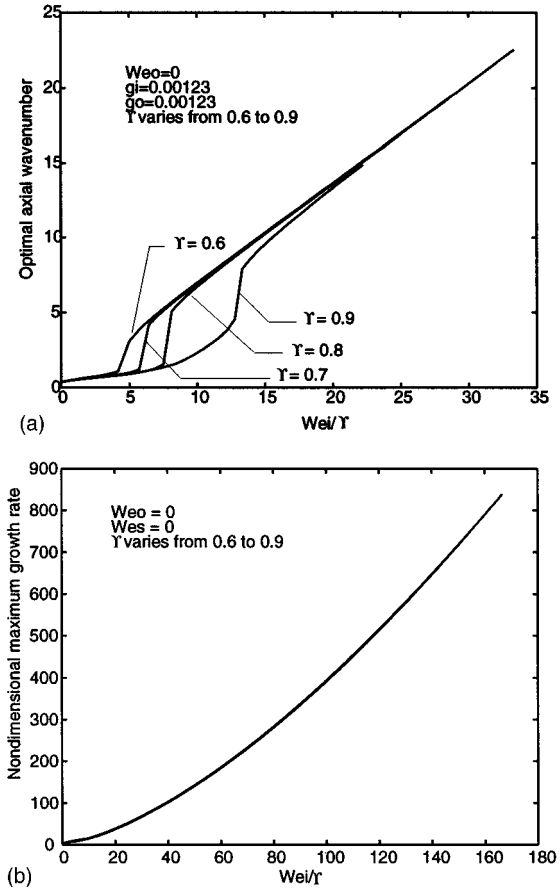

FIG. 5. (a) Optimal axial wavenumber versus We_i/γ for four radii ratios varying from 0.6 to 0.9. (b) Growth rate at an optimal wave mode versus We_i/γ for four radii ratios varying from 0.6. to 0.9.

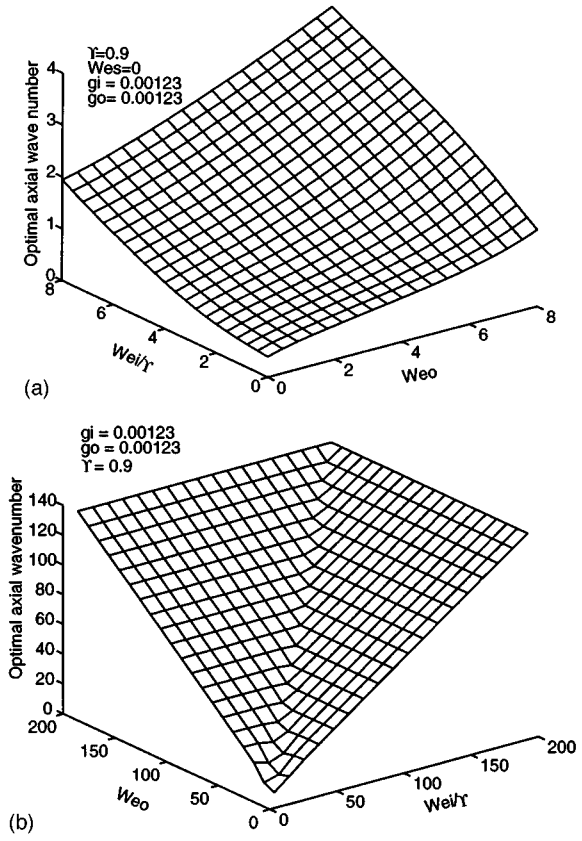

FIG. 6. (a) Optimal axial wavenumber versus the inside and outside Weber number at $g_i = g_o = 0.001\,23$ and $\gamma = 0.9$. (b) Optimal axial wavenumber versus We_i/γ and We_o at $\gamma = 0.9$ and $g_i = g_o = 0.000\,123$.

one another. The low and high We_i/γ behavior is due to breakup dominated by capillary and aerodynamic forces, respectively. There is also an intermediate region where the effect of radii ratio cannot be cast strictly in terms of We_i/γ. Behavior in this region is due to a competition between these two forces.

Growth rates corresponding to Fig. 5(a) optimal wavenumbers are illustrated in Fig. 5(b). Growth rate behavior differs from optimal wavenumber behavior in that there is no influence of γ on growth rate other than through the quotient We_i/γ.

Figure 6(a) is a plot of the optimal axial wavenumber versus We_i/γ and We_o for low values of Weber numbers (We_i/γ, $We_o < 8$). The radii ratio, γ, is 0.9 and the density ratios, g_i and g_o, are 0.001 23. The data show that the optimal wavenumber increases as either of the Weber numbers increase. However, the increase is slightly steeper when increasing We_i/γ than when increasing We_o. This indicates that it is slightly more efficient to use atomizing air on the inside of the annular sheet than on the outside at low Weber number atomizer operation. This conclusion provides at least a partial explanation for why effervescent atomizers produce drop sizes equal to those generated by prefilming airblast atomizers, but at lower air–liquid ratios by mass.[2,3,23,24]

Figure 6(b) is a plot of optimal axial wavenumber versus We_i/γ and We_o over the range of high Weber number values (We_i, $We_o \gg 1$) and for density ratios $g_i = g_o = 0.001\,23$ and $\gamma = 0.9$. The plot is symmetric about the line $We_i/\gamma = We_o$, indicating that aerodynamic forces, which dominate the breakup process at high Weber numbers, act equally inside or outside the sheet. Consequently, the optimal axial wavenumber is determined only by the maximum of the two Weber numbers, We_i/γ or We_o, so there appears to be no advantage of effervescent atomizers over conventional airblast or air-assist designs under these conditions.

Figure 7 is similar to Fig. 6(b), except that it is at $\gamma = 0.99$. As can be seen on comparison with Fig. 6(b), the optimal wavenumber at breakup exhibits the well-known decrease with increasing γ. Moreover, the plot is symmetric about $We_i/\gamma = We_o$, even at low Weber numbers. This indicates that the effect of We_i/γ is identical to that of We_o as the annular jet approaches a plane sheet, i.e., as γ tends to 1. Since γ is approaching unity, this means the effect of We_i is identical to that of We_o. This is expected due to the symmetry of a flat sheet.

Since the effect of We_o is smaller than that of We_i for small values of We_i and We_o, and since it is the maximum of We_i and We_o that determines optimal dimensionless wavenumber, kr_b, at high We_i and We_o, We_o has been set equal to zero in all the subsequent results without loss of generality.

Figure 8(a) is a plot of the optimal wavenumber versus

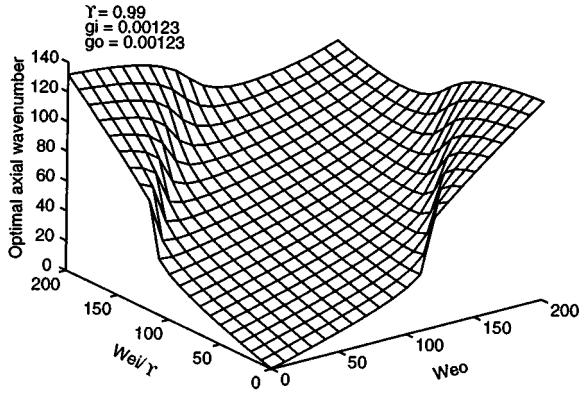

FIG. 7. Optimal axial wavenumber versus We_i/γ and We_o at $\gamma=0.99$ and $g_i=g_o=0.000\,123$.

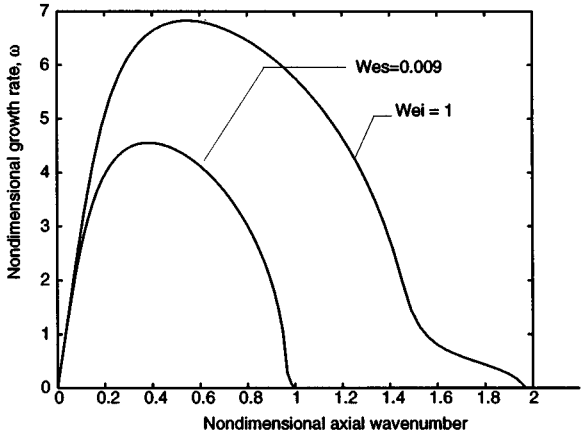

FIG. 9. Nondimensional growth rate versus nondimensional axial wavenumber for neutral stability of a pure swirling and pure axially flowing annular liquid sheet.

g_i and We_i at $\gamma=0.8$ and $We_o=0$. Figure 8(b) is a plot of the optimal wavenumber versus g_o and We_i at $\gamma=0.8$ and $We_o=0$. As Rangel and Sirignano[20] have shown for plane sheet stability, and has been verified for annular sheet stability by Lee,[5] antisymmetric disturbances dominate the breakup process below a critical density ratio. The range of density ratios considered in this study was therefore chosen such that the antisymmetric disturbance mode was dominant. This range also corresponds to that of engineering interest. As can be seen, density ratio has a minimal effect on the optimal wavenumber in the range of density ratios of engineering interest ($\frac{1}{800}$ to $\frac{1}{12}$, with the larger value corresponding to a diesel injector spraying into a combustion chamber at a typical operating pressure).

Figure 8(a) indicates that the effect of density ratio is two-fold. At very low Weber numbers ($We_i<5$), an increase in density ratio causes a very slight increase in optimal wavenumber. However, this effect is reversed as the Weber number increases—an increase in density ratio then causes a very slight decrease in the optimal wavenumber. Lund *et al.*[23] have made drop size measurements on effervescent sprays and noted that the drop size, which is a result of the optimal wavenumber at breakup, increases slightly as the atomizing gas molecular weight increases. Since an increase in optimal wavenumber corresponds to a decrease in ligament breakup length and, therefore, a reduction in mean drop size, the predictions of this analysis provide a partial explanation for the experimental measurements of Lund *et al.*[23]

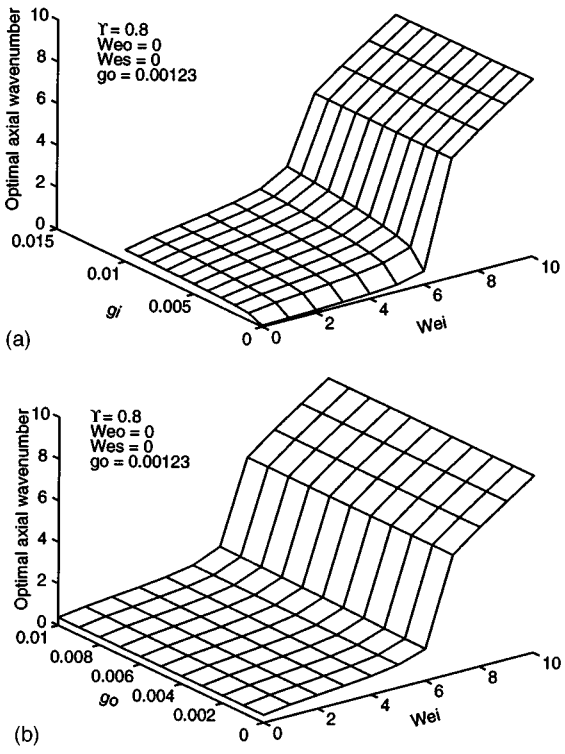

FIG. 8. (a) Optimal axial wavenumber versus density ratio of the gas phase inside and the Weber number inside. (b) Optimal axial wavenumber versus density ratio of the gas phase outside and the Weber number inside.

B. Effect of swirl

Swirl imposed on an annular liquid sheet has a dual effect on its stability. As Figs. 9 and 10 show, swirl has a

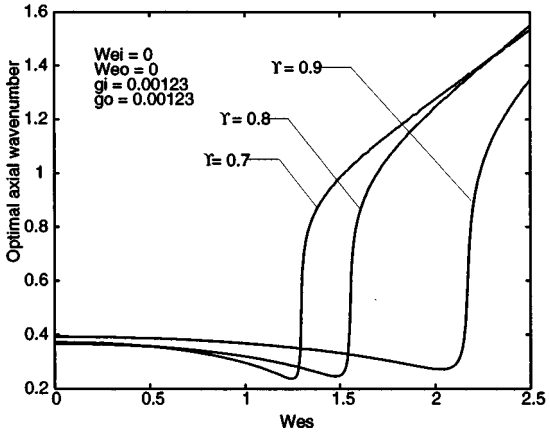

FIG. 10. Optimal axial wavenumber versus swirl Weber number for three radii ratios.

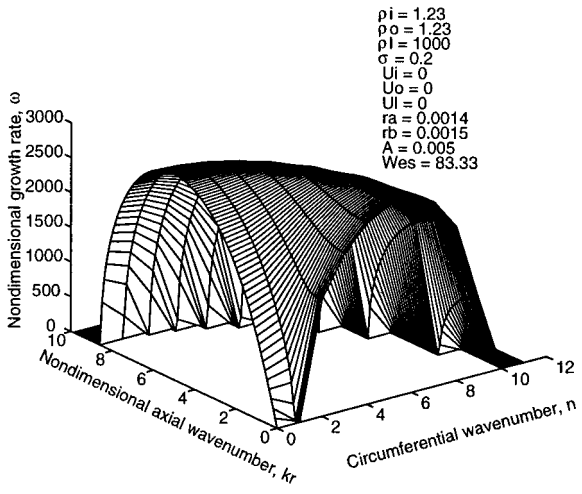

FIG. 11. Growth rate versus nondimensional axial and circumferential wavenumbers at $We_s=83.33$.

stabilizing effect at low values of swirl Weber number (~ 2), causing the optimal wavenumber and corresponding growth rates to decrease when compared to the pure axial flow case. However, as Figs. 11 and 12 show, swirl destabilizes the annular sheet at intermediate and high swirl Weber numbers.

Figure 9 is a plot of growth rate versus nondimensional axial wavenumber for two cases. The common feature of these two curves, and their basis for comparison, is the neutral stability of the first circumferential mode, i.e., the real part of the growth rate for the $n=1$ mode is exactly zero. In the first case, the liquid has no axial velocity and was swirling in a stationary gas field. The radii ratio, γ, was equal to 0.93. The swirl strength, A, was 8.68×10^{-5} m^2/s and $We_s=0.009$. (Recall that A is defined as the liquid phase swirl vortex strength and is used to define the mean circumferential velocity as A/r.) The second curve is similar to the first, but has $We_i=1.0$ and no swirl. As can be observed, the growth rates for the swirling case are lower than for the pure axial flow case and the shape of the swirling flow curve is shifted toward lower wavenumbers. Swirl is therefore seen to stabilize the annular sheet at low values of swirl Weber number.

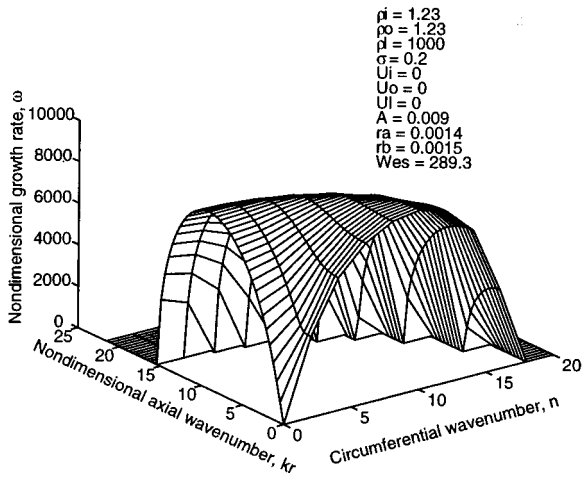

FIG. 12. Growth rate versus nondimensional axial and circumferential wavenumbers at $We_s=259.3$.

Figure 10 is a plot of the optimal wavenumber versus swirl Weber number at low values of swirl Weber number in the absence of relative axial velocity for radii ratios of 0.7, 0.8, and 0.9. The range of swirl Weber numbers on this plot is limited to cases where only the $n=0$ disturbance mode has the maximum growth rate. Two regions can be identified: the initial region, where the optimal dimensionless axial wavenumber decreases with We_s, and a region of monotonic increase of kr_b with an increase in We_s. The first region occurs at low values of swirl Weber number and the decrease in kr_b shows that small amounts of swirl stabilize the flow in a practical sense. In other words, small amounts of swirl shift the optimal disturbance mode to lower wavenumbers, which in turn leads to longer ligament breakup lengths and larger drops. This effect is most prominent at high values of γ, precisely the conditions most likely to occur in a practical prefilming airblast, air-assist, or pressure-swirl atomizer. Consequently, there exists a critical swirl Weber number below which operating a nozzle is undesirable. The value of this critical swirl Weber number at each γ is determined by the minimum of the corresponding curve. This minimum occurs at low Weber numbers because of a competition between the restorative centrifugal force and the disruptive capillary force. The aerodynamic force is negligible under these conditions.

Figure 11 is a plot of dimensionless growth rate versus nondimensional axial and circumferential wavenumbers at a swirl Weber number of 83.33. Note that the maximum growth rate occurs at a finite value of the axial wavenumber and at circumferential wavenumber $n=0$, just as in the nonswirling case. However, on comparison with Fig. 3, we observe that the growth rates in Fig. 11 are approximately constant over almost the entire range of unstable disturbance modes, while the dispersion diagram is more rounded in Fig. 3. This qualitative difference is ascribed to the different mechanisms by which axial velocity and swirl act to amplify nonaxisymmetric modes at high swirl Weber numbers.

Of more interest is the practical case when nonlinear behavior becomes important. Under those conditions we would expect to see more complicated breakup structures (i.e., modes where both n and $k>0$) when swirl is present than when it is absent. This is due to the large number of waves growing at approximately the same rate in the swirling case.

Figure 12 was obtained for $We_s=289.3$. It is qualitatively similar to Fig. 11, but the range of unstable axial and circumferential wavenumbers has increased, as has the magnitude of the nondimensional growth rate for the fastest growing mode. The most striking difference between Figs. 11 and 12 is the shift in optimal disturbance mode from (kr_b,n) of $(\sim 7.5,0)$ to (kr_b,n) of $(0,10)$.

Figures 13(a) and 13(b) are plots of optimal dimensionless axial and circumferential wavenumbers versus We_s and We_i for $0<We_s,We_i<10$. These figures demonstrate the

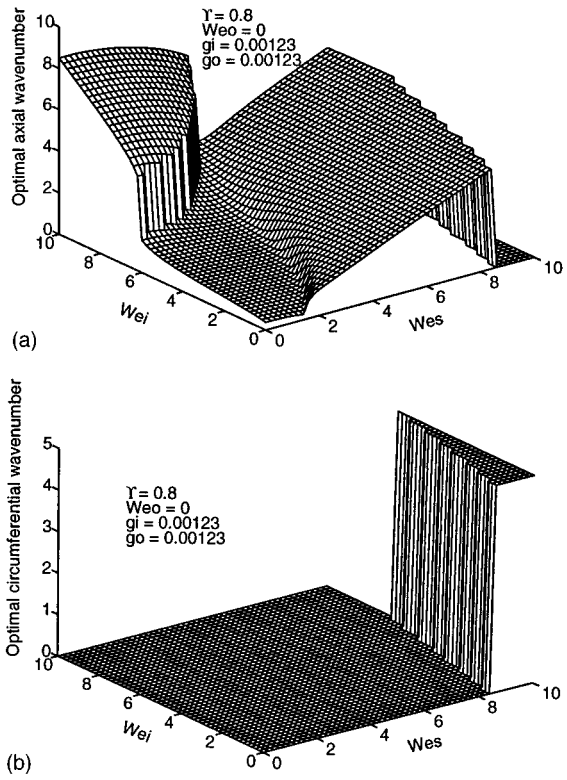

FIG. 13. (a) Optimal axial wavenumber versus axial and swirl Weber numbers. (b) Optimal circumferential wavenumber versus axial and swirl Weber numbers.

various asymptotic regimes that are present in annular sheet stability.

When $We_i \gg We_s$, the optimal disturbance mode occurs at $n=0$ and a finite value of the axial wavenumber. When $We_s \gg We_i$, the optimal disturbance mode occurs at $kr_b=0$ and a finite value of the circumferential wavenumber. Both types of behavior are similar to that of a liquid flow bounded by infinite parallel walls, as reported by Squire.[19] Squire[19] noted that it was sufficient to confine attention to two-dimensional disturbances oriented along the primary flow direction.

Figure 13(a) is a plot of optimal axial wavenumber versus inner and swirl Weber numbers. It contains data already presented in Figs. 5(a) and 10 when We_s and We_i are zero, respectively.

Figure 13(a) indicates that the two regions of optimal axial wavenumber behavior observed in Fig. 10 also exist for $We_i>0$. However, as We_i increases, the decrease in optimal axial wavenumber with an increase in We_s becomes quite pronounced. Figure 13(a) also indicates the presence of a third optimal axial wavenumber region. For instance, the fastest growing mode has a circumferential wavenumber of $n=0$ for $We_i=0$ and We_s less than 8.4. A further increase in We_s above 8.4 results in the optimal disturbance mode shifting from $n=0$ and finite values of kr_b to $kr_b=0$ and finite values of n [see Fig. 13(b)]. Furthermore, the swirl Weber number at which the fastest growing mode retains a circumferential wavenumber of $n=0$ increases as We_i increases. A critical swirl Weber number can therefore be identified for each value of We_i, γ, We_o, and density ratios that is required for the optimal disturbance mode to shift from $n=0$ to a finite n. Finally, a further increase in the swirl Weber number after the optimal disturbance mode has shifted to $k=0$ results in an increase in the optimal dimensionless circumferential wavenumber.

The regime where $n>0$ is of most interest for practical atomizer operation because this is where an increase in annular sheet swirl directly affects the number of ligaments formed and, consequently, the drop size. For example, increasing the swirl Weber number increases the number of ligaments and decreases their diameters. A decrease in ligament diameter leads to a corresponding decrease in ligament breakup length and, hence, a reduction in drop size. This relationship between annular sheet swirl and drop size is well known.[2]

Figures 14(a)–14(c) are plots of nondimensional growth rate versus nondimensional axial and circumferential wavenumbers for three cases with $\gamma=0.6$. All three figures show the interesting feature of two distinct regions of instability, each with its own local nondimensional growth rate maximum. Figure 14(a) was generated at an axial Weber number ($We_i=150.0$) such that the effect of axial velocity on the disturbance growth behavior was less than the effect of liquid swirl—note that the peak growth rate due to the axial Weber number (along the axial wavenumber, or $n=0$, axis) is less than the peak growth rate due to swirl (along the circumferential wavenumber, or $kr_b=0$, axis). As the axial Weber number is increased, the peak growth rate due to the axial Weber number increases until it reaches a condition where the two local maxima have the same value [see Fig. 14(b)]. As the axial Weber number is increased further still, the relative magnitudes of the axial and circumferential maxima shift and the axial maximum becomes the larger of the two.

The amount of swirl required to cause the optimal disturbance mode to shift from $n=0$ to $n>0$ is small and could typically be present in a practical atomizer because of imperfections in nozzle geometry or two-phase flow fluctuations. For example, a swirl Weber number of 80 and an axial Weber number of 4 result in a spray cone angle of about 8°, which is typical of effervescent atomizer-produced sprays. Consequently, the presence of small fluctuations in swirl velocity could cause the annular sheet to disintegrate into a finite number of ligaments, as observed by Santangelo and Sojka.[3] However, in a more controlled environment where swirl is almost absent, such as the experiments of Kendall,[4] the annular sheet is expected to break up into toroidal rings. Both these mechanisms are predicted by the model developed here.

Regardless of the relative magnitudes of the axial and swirl Weber numbers, the two instability regions are separated by a domain where all instabilities are damped. The presence of two distinct regions of instability differs from the observations of all previous investigators whose analyses predicted a single, simply connected, instability region.

Figures 15(a)–15(c) are similar to Figs. 14(a)–14(c), except that they are at a radii ratio of $\gamma=0.9$. Figure 15(a) is generated at an axial Weber number lower than the crossover

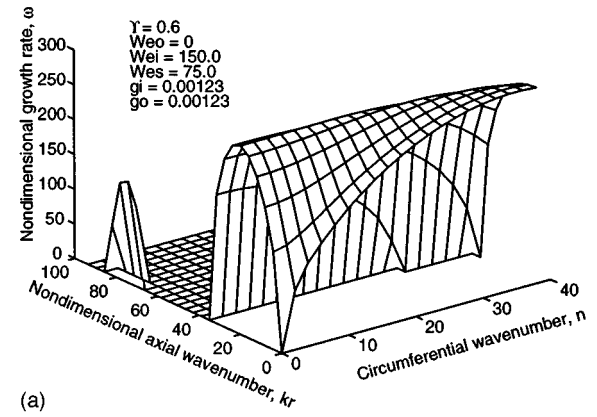

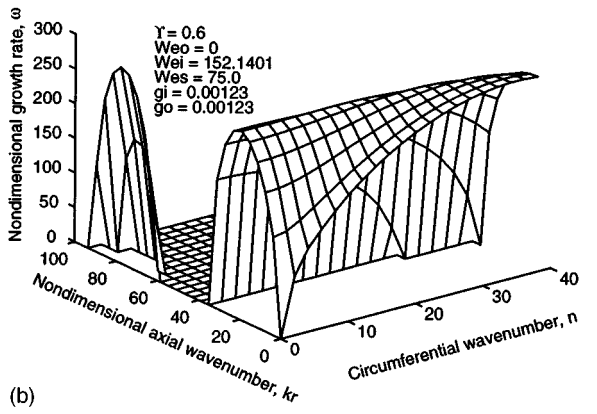

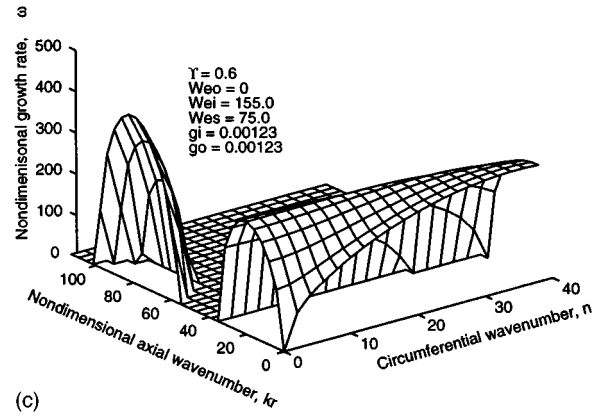

FIG. 14. (a) Nondimensional growth rate versus axial and circumferential wavenumbers for $We_i=150.0$, $We_s=75.0$, and $\gamma=0.6$. (b) Nondimensional growth rate versus axial and circumferential wavenumbers for $We_i=152.1401$, $We_s=75.0$, and $\gamma=0.6$. (c) Nondimensional growth rate versus axial and circumferential wavenumbers for $We_i=155.0$, $We_s=75.0$, and $\gamma=0.6$.

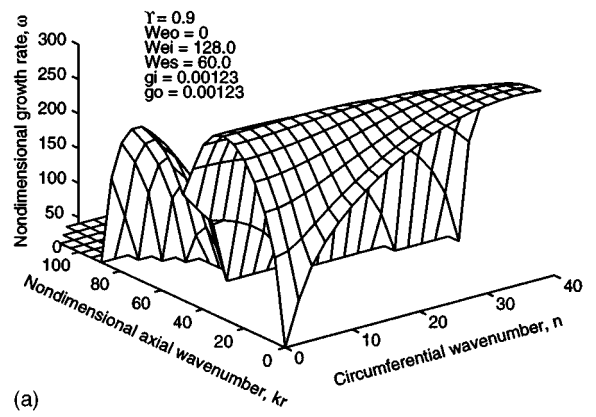

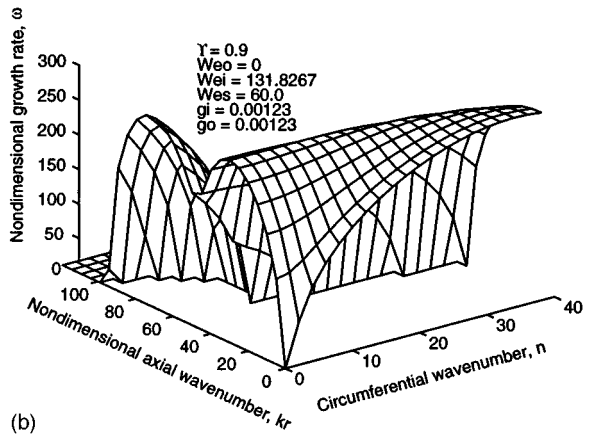

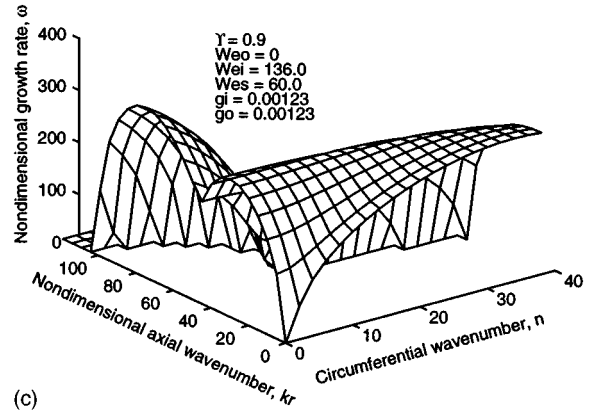

FIG. 15. (a) Nondimensional growth rate versus axial and circumferential wavenumbers for $We_i=128.0$, $We_s=60.0$, and $\gamma=0.9$. (b) Nondimensional growth rate versus axial and circumferential wavenumbers for $We_i=131.8267$, $We_s=60.0$, and $\gamma=0.9$. (c) Nondimensional growth rate versus axial and circumferential wavenumbers for $We_i=136.0$, $We_s=60.0$, and $\gamma=0.9$.

value, Fig. 15(c) was generated at a Weber number higher than the crossover value, and Fig. 15(b) was generated at a Weber number equal to the crossover value (the crossover Weber number is where the magnitudes of the axial and circumferential velocity modes are equal). We see from these figures that the behavior follows that shown in Figs. 14(a)–14(c): the optimal disturbance mode, which occurs along the $kr_b=0$ axis [Fig. 15(a)] at low values of axial Weber number, shifts to the $n=0$ axis [Fig. 15(c)] as the axial Weber number increases to a value above the crossover point. At the crossover point, the dispersion diagram exhibits two maxima having exactly the same growth rate, one occurring along $n=0$ and one along $kr_b=0$.

Comparison of Figs. 14 and 15 illustrates two qualitative differences. At low values of γ, i.e. when the annular sheet is thick, the effects of relative axial velocity between the gas and liquid phases and the effect of swirl can be separately identified as two distinct instability regions. However, as γ increases, i.e. as the sheet gets thinner, the regions due to relative axial velocity and swirl merge into a single, simply connected, instability domain.

The critical condition when the dispersion diagram has

two maxima of identical magnitude [see Figs. 14(b) and 15(b)] is important because instabilities in the axial and circumferential direction grow at the same rate. This critical condition can be identified as a particular axial Weber number, We_i, for a given set of g_i, g_o, We_o, We_s, and γ.

The key feature of Figs. 14(b) and 15(b) is that each contains two local maxima with identical growth rates. The optimal disturbance mode can therefore be written as a superposition,

$$r = r_b + \eta_0 \cos(k^* z) + \eta_0 \cos(n^* \theta), \tag{17}$$

where k^* and n^* are the k and n values for the peaks at $(k,0)$ and $(0, n)$. Choosing

$$\xi = \frac{1}{2}\left(z - \frac{n^*}{k^*}\,\theta\right) \tag{18}$$

and

$$\phi = \frac{1}{2}\left(\frac{k^*}{n^*}\,z + \theta\right), \tag{19}$$

the optimal disturbance mode can be rewritten as

$$r = r_b + \eta_0 \cos(k^* \xi)\cos(n^* \phi), \tag{20}$$

demonstrating the three-dimensional nature of these modes.

If results of the linear analysis can be used as a qualitative indicator of a practical breakup process, the presence of a critical conditions in Figs. 14(b) and 15(b) suggests that, under nonlinear conditions, the annular sheet under will break up into a finite number of ligaments of finite length, as observed by Santangelo and Sojka[3] in their holograms (Fig. 1).

IV. SUMMARY AND CONCLUSIONS

A linear model describing the instability behavior of annular, swirling, inviscid sheets subject to inner and outer gas flows of differing velocities is presented. Model predictions show the following.

(1) In the absence of swirl, an increase in axial Weber number causes the range of unstable axial disturbance modes to increase significantly. However, the disturbance mode having the maximum growth rate always has a circumferential mode number of zero.

(2) In the absence of swirl and when the axial Weber numbers, We_i, are small (<8), the inner gas flow leads to slightly faster growing axial instability modes than the outer gas flow at equivalent inner and outer Weber numbers (We_i and We_o). This observation provides a partial explanation of why effervescent atomizers require less atomizing gas than conventional twin-fluid injectors (such as airblast and air-assist) when producing sprays having the same mean drop size. However, inner and outer gas flows have the same effect when the inner and outer Weber numbers are high ($We_i, We_o > 10$). This suggests that the performance of conventional twin-fluid atomizers will approach that of effervescent atomizers at sufficiently high Weber numbers.

(3) When swirl is absent, the wavenumber for the axial mode having the highest growth rate decreases with an increase in surface tension. This behavior is qualitatively the same as that reported by previous researchers who considered only one-dimensional disturbances.[5]

(4) When there is no swirl, an increase in the density of the atomizing gas results in a slight increase in the wavenumber of the axial disturbance mode having the highest growth rate. This finding provides a partial explanation for the reduction in effervescent atomizer-produced spray mean drop size with an increase in atomizing gas molecular weight.[23]

(5) For axial Weber numbers (We_i, We_o) of zero, swirl reduces the wavenumber for the axial disturbance mode having the highest growth rate and reduces growth rates as well. This observation may provide a partial explanation for the rapid rise in mean drop size exhibited by pressure-swirl atomizer produced sprays when the atomizer swirl number is reduced.

(6) For nonzero axial Weber numbers (We_i, We_o), an increase in the swirl Weber number, We_s, increases the range of unstable axial and circumferential modes and increases growth rates as well. In addition, the instability surface is much more rounded, i.e. a larger number of modes have nearly equal growth rates, when swirl is present than when swirl is absent. This suggests that nonlinear effects are more likely to occur for the swirling case.

(7) Increasing the swirl Weber number, We_s, increases the axial wavenumber for the disturbance mode having the highest growth rate, but a circumferential mode number of zero is retained until We_s exceeds about 8. At this point, the axial wavenumber for the disturbance having the highest growth rate falls to zero and the circumferential wavenumber jumps to a finite value of n. Further increases in We_s serve to increase n.

(8) Up to two local nondimensional growth rate maxima can exist, and the instability domain can be simply connected or can consist of two separate regions separated by an area where disturbances are stable. The topology of the growth rate surface depends on the ratio of the annulus inner (r_a) to outer (r_b) radii: two separate regions exist when the annulus is thick, i.e. a radii ratio of 0.6, while only one region exists when the annulus is thin, i.e. a radii ratio of 0.9. Furthermore, the relative magnitudes of the local growth rate maxima can be matched by correct choice of axial (We_i, We_o) and swirl (We_s) Weber numbers. High axial Weber numbers result in the local growth rate maximum for the region having a circumferential wavenumber of zero to be the global maximum while high swirl Weber numbers result in the local growth rate maximum for the region having an axial wavenumber of zero to be the global maximum. Finally, the axial and swirl Weber numbers can be adjusted so that the two growth rate maxima have equal values. Three-dimensional disturbances exist for this case.

(9) The sheet is always unstable to two-dimensional disturbances. These may take either an axial or circumferential form. Most importantly, model predictions demonstrate that the sheet can be unstable to three-dimensional disturbances if the axial (We_i, We_o) and swirl (We_s) Weber numbers are correctly chosen.

APPENDIX: DISPERSION RELATION COEFFICIENTS

The dispersion relation that results from the linear stability analysis of an inviscid swirling annular liquid sheet in the presence of inviscid nonswirling gas inside and outside that move with unequal velocities is presented here. It is the equation derived in Sec. II A.

The dispersion relation given by (16) is a polynomial of the form

$$a_4(k,n)\omega^4+a_3(k,n)\omega^3+a_2(k,n)\omega^2+a_1(k,n)\omega + a_0(k,n)=0, \tag{A1}$$

where

$$a_4(k,n)=C_1C_4+C_7C_{10},$$
$$a_3(k,n)=C_1C_5+C_2C_4+C_7C_{11}+C_8C_{10},$$
$$a_2(k,n)=C_1C_6+C_2C_5+C_7C_{12}+C_8C_{11}+C_9C_{10},$$
$$a_1(k,n)=C_3C_5+C_2C_6+C_8C_{12}+C_9C_{11},$$
$$a_0(k,n)=C_3C_6+C_9C_{12}.$$

The coefficients C_i are given by,

$$C_1=\frac{\rho_o}{k}G_n-\frac{\rho_l}{k}B_n,$$

$$C_2=2i\rho_oU_{zo}G_n-2i\frac{\rho_l}{k}\left(\frac{nA}{r_b^2}+kU_{zl}\right)B_n,$$

$$C_3=-\rho_oU_{zo}^2kG_n+\frac{\rho_l}{k}\left(\frac{nA}{r_b^2}+kU_{zl}\right)^2B_n+\frac{\sigma}{r_b^2}\times[1-n^2-(kr_b)^2]+\frac{\rho_lA^2}{r_b^3},$$

$$C_4=-\frac{\rho_i}{k}H_n-\frac{\rho_l}{k}C_n,$$

$$C_5=-2i\rho_iU_{zi}H_n-2i\frac{\rho_l}{k}\left(\frac{nA}{r_a^2}+kU_{zl}\right)C_n,$$

$$C_6=\rho_iU_{zi}^2kH_n+\frac{\rho_l}{k}\left(\frac{nA}{r_a^2}+kU_{zl}\right)^2C_n+\frac{\sigma}{r_a^2}\times[1-n^2-(kr_a)^2]-\frac{\rho_lA^2}{r_a^3},$$

$$C_7=\frac{\rho_l}{k}S_n,$$

$$C_8=i\frac{\rho_l}{k}\left(\frac{nA}{r_a^2}+\frac{nA}{r_b^2}+2kU_{zl}\right)S_n,$$

$$C_9=-\frac{\rho_l}{k}S_n\left(\frac{nA}{r_a^2}+kU_{zl}\right)\left(\frac{nA}{r_b^2}+kU_{zl}\right),$$

$$C_{10}=\frac{\rho_l}{k}Q_n,$$

$$C_{11}=i\frac{\rho_l}{k}\left(\frac{nA}{r_a^2}+\frac{nA}{r_b^2}+2kU_{zl}\right)Q_n,$$

$$C_{12}=-\frac{\rho_l}{k}Q_n\left(\frac{nA}{r_a^2}+kU_{zl}\right)\left(\frac{nA}{r_b^2}+kU_{zl}\right),$$

where

$$B_n=\frac{[I_n'(kr_a)K_n(kr_b)-I_n(kr_b)K_n'(kr_a)]}{[I_n'(kr_a)K_n'(kr_b)-I_n'(kr_b)K_n'(kr_a)]},$$

$$C_n=\frac{[I_n'(kr_b)K_n(kr_a)-I_n(kr_a)K_n'(kr_b)]}{[I_n'(kr_a)K_n'(kr_b)-I_n'(kr_b)K_n'(kr_a)]},$$

$$S_n=\frac{[I_n'(kr_b)K_n(kr_b)-I_n(kr_b)K_n'(kr_b)]}{[I_n'(kr_a)K_n'(kr_b)-I_n'(kr_b)K_n'(kr_a)]},$$

$$Q_n=\frac{[I_n(kr_a)K_n'(kr_a)-I_n'(kr_a)K_n(kr_a)]}{[I_n'(kr_a)K_n'(kr_b)-I_n'(kr_b)K_n'(kr_a)]},$$

$$G_n=\frac{K_n(kr_b)}{K_n'(kr_b)},$$

$$H_n=\frac{I_n(kr_a)}{I_n'(kr_a)}.$$

The prime denotes differentiation with respect to the argument of the Bessel functions I_n and K_n.

[1] J. Ponstein, ''Instability of rotating cylindrical jets,'' Appl. Sci. Res. A **8**, 425 (1959).
[2] A. H. Lefebvre, *Atomization and Sprays* (Hemisphere, New York, 1989).
[3] P. J. Santangelo and P. E. Sojka, ''A holographic investigation of the near-nozzle structure of an effervescent atomizer-produced spray,'' Atom. Sprays **5**, 137 (1995).
[4] J. M. Kendall, ''Experiments on annular liquid jet instability and on the formation of liquid shells,'' Phys. Fluids **29**, 2086 (1986).
[5] J. G. Lee, ''Breakup of cylindrical liquid sheets,'' Ph.D. thesis, University of Iowa, 1990.
[6] J. H. Dumbleton and J. J. Hermans, ''Capillary instability of a hollow inviscid cylinder,'' Phys. Fluids **13**, 12 (1970).
[7] G. D. Crapper, N. Dombrowski, and G. A. D. Pyott, ''Kelvin–Helmholtz wave growth on cylindrical sheets,'' J. Fluid Mech. **68**, 497 (1975).
[8] P. D. Esser, D. D. Paul, and S. I. Abdel-Khalik, ''Stability of the lithium 'waterfall' first wall protection concept for inertial confinement fusion reactors,'' Nucl. Technol. Fusion **1**, 285 (1981).
[9] J. Meyer and D. Weihs, ''Capillary instability of an annular liquid jet,'' J. Fluid Mech. **179**, 531 (1987).
[10] M. Harvanek and C. Chow, ''Electromagnetic-capillary instability of a liquid cylinder. Production of spherical shells,'' AIAA J. **28**, 372 (1990).
[11] J.-G. Lee and L.-D. Chen, ''Linear stability analysis of gas–liquid interface,'' AIAA J. **29**, 1589 (1991).
[12] N. Dombrowski and W. R. Johns, ''The aerodynamic instability and disintegration of viscous liquid sheets,'' Chem. Eng. Sci. **18**, 203 (1963).
[13] M. V. Panchagnula, P. J. Santangelo, and P. E. Sojka, ''The instability of an inviscid annular liquid sheet subject to two-dimensional disturbances,'' in *Proceedings ILASS Americas '94*, 8th Annual Conference on Liquid Atomization and Spray Systems, Troy, MI, pp. 54–58.
[14] W. C. Nieuwkamp, ''Flow analysis of a hollow cone nozzle with potential flow theory,'' paper IIIC/1 in *Proceedings of ICLASS-85*, the 3rd International Conference on Liquid Atomization and Spray Systems (Institute of Energy, London, UK, 1986).
[15] J. Shen and X. Li, ''Instability of an annular viscous liquid jet,'' Acta Mech. **114**, 167 (1996).
[16] R. H. Rangel and W. A. Sirignano, ''The linear and nonlinear shear instability of a fluid sheet,'' Phys. Fluids A **3**, 2392 (1991).
[17] A. M. Sterling and C. A. Sleicher, ''The instability of capillary jets,'' J. Fluid Mech. **68**, 477 (1975).
[18] S. Chandrasekhar, *Hydrodynamic and Hydromagnetic Stability* (Dover, New York, 1961).
[19] H. B. Squire, ''Investigation of the instability of a moving liquid film,'' Br. J. Phys. A **4**, 167 (1953).

[20]R. H. Rangel and W. A. Sirignano, ''Nonlinear growth of Kelvin–Helmholtz instability: Effect of surface tension and density ratio,'' Phys. Fluids **31**, 1845 (1988).
[21]A. E. Radwan, ''Nonaxisymmetric magnetohydrodynamic instability of a streaming bounded hollow cylinder,'' J. Magn. Magn. Mat. **92**, 233 (1990).
[22]A. E. Radwan, ''Three dimensions varying MHD instability of an annular fluid cylinder,'' J. Magn. Magn. Mat. **94**, 319 (1991).
[23]M. T. Lund, C. Q. Jiang, P. E. Sojka, J. P. Gore, and M. V. Panchagnula, ''Effect of atomizing gas molecular weight on effervescent atomizer performance,'' submitted to ASME J. Fluids Eng.
[24]M. T. Lund, P. E. Sojka, A. H. Lefebvre, and P. G. Gosselin, ''Effervescent atomization at low mass flow rates. Part I: The influence of surface tension,'' Atom. Sprays **3**, 77 (1993).